Materials & Design 185 (2020) 108237

Contents lists available at ScienceDirect

Materials & Design

journal homepage: www.elsevier.com/locate/matdes

Rapid fabrication of perovskite solar cells through intense pulse light annealing of SnO_2 and triple cation perovskite thin films

Amir H. Ghahremani [a, b], Blake Martin [c], Alexander Gupta [c], Jitendra Bahadur [d], Krishnamraju Ankireddy [a], Thad Druffel [a, *]

[a] University of Louisville, Conn Center for Renewable Energy Research, Louisville, KY, 40292, USA
[b] University of Louisville, Department of Mechanical Engineering, Louisville, KY, 40292, USA
[c] University of Louisville, Department of Chemical Engineering, Louisville, KY, 40292, USA
[d] Centre of Nanotechnology, Indian Institute of Technology Roorkee, Roorkee, 247667, India

HIGHLIGHTS

- Sequential step IPL annealing, SnO_2, Perovskite film, Perovskite solar cell, Rapid thermal annealing.
- Di-iodomethane (CH_2I_2) was shown to be compatible and improve the quality of fabricated films derived from other perovskite chemistries such as mixed triple cation precursors.
- Pulse count and the heat flux per pulse was shown to play a significant role on SnO_2 charge extraction.

GRAPHICAL ABSTRACT

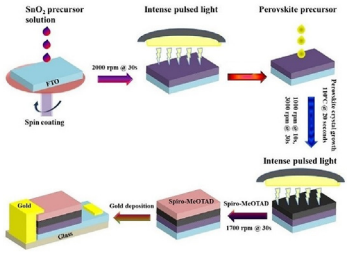

ARTICLE INFO

Article history:
Received 27 June 2019
Received in revised form
23 September 2019
Accepted 24 September 2019
Available online 11 October 2019

Keywords:
Intense pulse light
Rapid thermal annealing
Di-iodomethane
SnO_2
Perovskite solar cell

ABSTRACT

Rapid evolution of perovskite solar cells (PSCs) performance and stability has inclined the research focus towards scalable bulk fabrication through high speed and cost-effective automated methods. For the first time, intense pulsed light (IPL) is utilized to rapidly fabricate efficient PSCs through swift annealing of both the SnO_2 electron transport layer (ETL) and mixed triple cation perovskite thin films. The addition of di-iodomethane (CH_2I_2) alkyl-halide could enhance the PSC efficiency by retarding the crystallization and improving the surface morphology of the perovskite photoactive film through supplying iodine cleaved by ultraviolet energy during IPL process. The maximum efficiency and fill factor of the PSCs fabricated by IPL annealing were 12.56% and 78.3% for the rigid glass-FTO slides, and 7.6% and 64.75% for flexible PET-ITO substrates when processed in the ambient with relative humidity of 60%, respectively. The annealed materials were characterized through Scanning electron microscopy (SEM), UV–Vis, photoluminescence (PL), X-ray diffraction (XRD), and X-ray photoelectron spectroscopy (XPS) techniques. In addition, impedance spectroscopy (IS) and current-voltage measurements were conducted to study the functionality of fabricated cells. Our results delineated the feasibility of sequential step IPL annealing on rapid fabrication of efficient PSCs which is directly applicable for scalable roll-to-roll manufacturing.

1. Introduction

In less than a decade, the organic-inorganic PSCs with the general structure of ABX_3 (A = methylammonium ($MA = CH_3NH_3^+$),

* Corresponding author.
E-mail address: Thad.druffel@louisville.edu (T. Druffel).

https://doi.org/10.1016/j.matdes.2019.108237

formamidinium ($FA{=}CH_3(NH_2)_2^+$), cesium (Cs^+), or rubidium (Rb^+) [1]; B= Pb^{2+}, Sn^{2+} or Ge^{2+}; and X = Cl^-, Br^-, I^- halides or mixture thereof, as well as a non-halide compounds such as acetates [2]) have undergone a dramatic efficiency improvement from 3.8% [3] to over 23% [4]. Such staggering achievements have been credited to the perovskite tunable bandgap [5], ultraviolet (UV) to infrared (IR) light absorption range [6], high charge mobility [7], long carrier diffusion length [8], exciton low binding energy [9], acute optical band edge [10], and bipolar semi-conductivity [11]. Rapid enhancements within these domains have made PSCs a viable opportunity toward bulk manufacturing using simple deposition and processing methods with the potential to rival silicon photovoltaics. So far, most of the investigations have been focused on four major fields such as ink engineering [12,13]; thin film deposition methods such as spray coating [14–17], slot-die coating [18–21], blade coating [22], gravure coating [23,24], and inkjet printing [25–27]; annealing methods such as hotplate [28], hot air blowing [29], and radiative annealing [30]; and fabrication techniques such as two-step coating [31], anti-solvent dripping [32], gas quenching [33], vacuum-flash assisted [34], and vapor assisted solution processing [35]. Despite dramatic progress within these areas, crucial processes are impeding full and rapid roll to roll manufacturing of PSCs. Aside from moisture and thermal stability concerns [36–40], rapid cost-effective annealing of the perovskite and ETL has remained a challenge for high throughput roll-to-roll manufacturing of PSCs.

To date, PSCs have been fabricated by taking the advantage of high temperature annealed metal-oxide electron transport layers (ETLs), such as ZnO, TiO_2 or SnO_2, in a furnace (up to 500 °C) for approximately an hour [41,42], or have been annealed through medium temperature ranges (~150 °C) within minutes time frame [43–45]. Prolonged annealing of PSCs not only doesn't meet the energy payback time [46], but also necessitates the application of long ovens, batched ovens, or lowered web speeds within the roll-to-roll setup. In addition, the prolonged heat treatment using temperatures greater than 150 °C is a hindrance to the application of roll-to-roll favorable PET flexible substrates. Therefore, taking advantage of cost effective and rapid annealing processes for the charge carrier and perovskite films is a crucial factor for roll-to-roll manufacturing of PSCs.

Intense pulsed light (IPL) is an economical roll-to-roll applicable method which can be used for rapid thermal processing of various thin films [47–52]. IPL anneals PSC thin films through energetic flashes of light, typically from a xenon lamp, within millisecond time frame to crystallize the material without damaging the underneath layers. Lavery et al. applied IPL on $MAPbI_3$ perovskite thin films deposited on high temperature furnace sintered compact and mesoporous TiO_2 ETL by discharging a single shot, up to 2000 J of energy per pulse, and reported increased efficiencies from 8.21% to 11.5% compared to the fully hotplate annealed perovskite films [53]. Zhu et al. also reported rapid sintering of SnO_2 ETL derived from a solution of $SnCl_4$ in ultra-pure water and reported 15.3% efficiency after 20 ms light exposure with the total energy of 46 J/cm^2 [54]. Das et al. successfully sintered TiO_2 films deposited on PET flexible substrates using 5 infrared pulses with 2 ms pulse dwell time to create efficient $CH_3NH_3PbI_{3-x}Cl_x$ solar cells after one hour hotplate annealing of the perovskite films at 100 °C [55]. Recently, Duo et al. successfully produced roll-to-roll printed PSCs, reaching to 19.6% PCE [20]. However, they annealed the SnO_2 ETL at 220 °C through two ovens, each having one meter length, and created the perovskite films by heating the substrates for 10 min at 130 °C. Despite such improvements, none of these investigations managed high throughput processing of both the ETL and perovskite films which would make them feasible for rapid and continuous automated manufacturing. Successful fabrication of efficient PSCs necessitates production of thin films which possess superior morphology and optimal material crystallization based on optimum thermal annealing and tuned ink engineering [56,57].

In this paper, we have rapidly processed PSCs from a $Cs_{0.05}(MA_{0.85}FA_{0.15})_{0.95}PbI_3$ mixed triple cation perovskite ink with CH_2I_2 alkyl-halide additive, in which, the ETL and the perovskite photoactive films were made through a single step spin-coating, both on rigid glass-FTO and flexible PET-ITO substrates, and were subsequently annealed using millisecond duration pulses from a Xenon lamp. The ink engineering and coating parameters were tuned in a manner which could deliver adequate wet film quality before the annealing process and mirror-like films with superior morphology and high crystallinity after the annealing process in the ambient with relative humidity about 60%. This study was conducted by initially finding the suitable pulse energy and counts for the optimum annealing of SnO_2 ETL on rigid glass-FTO slides, studying the impact of CH_2I_2 on the perovskite film quality, and, finally, applying the optimized conditions to make PSCs on both the rigid FTO coated glass and roll-to-roll applicable PET-ITO flexible substrates. The morphological inspection of thin films was carried out using SEM, the structural properties were investigated using XPS and XRD techniques, PL and IS were used to examine the interfacial charge transport capability, and current-voltage curves were obtained to measure the device performance. Our results provided rapid cost-effective fabrication of efficient PSCs without any further dopants or treatments which can be directly implemented for a low cost and scalable fabrication of PSCs through roll to roll.

2. Experimental section

2.1. Materials

Unless noted otherwise, all materials were purchased from Sigma Aldrich without further purification. PbI_2 (99.9985%), *N*,*N*-Dimethylformamide (99.8%), di-iodomethane (99%), and SnO_2 solution (15% in H_2O colloidal dispersion) were purchased from Alfa Aesar. Methylammonium iodide (MAI), Formamidinium iodide (FAI), and cobalt dopant FK209 were purchased from Greatcell solar. The 2,20,7,70-Tetrakis(*N*,*N*-di-*p*-methoxyphenylamine)-9,90-spirobifluorene (Spiro-MeOTAD) was acquired from Merck. FTO glass substrates (<20 Ω/sq., 2 cm × 2 cm × 3 mm) and gold palettes (99.999%) were purchased from Hartford glass and Kurt J. Lesker Co., respectively. ITO coated PET sheets (60 Ω/sq.) were purchased from Sigma Aldrich.

2.2. Device fabrication

FTO/ITO coated slides (2 cm × 2 cm) were initially etched using zinc powder and 2 M HCl and were subsequently cleaned through sequential sonication in a 1:10 V/V diluted solution of Hellmanex detergent in DI water, DI water, ethanol, and DI water for 10 minutes each. After blowing with nitrogen to remove the remainder water, 20 minutes plasma treatment was applied to the cleaned substrates to improve the surface energy and thus the hydrophilicity. The SnO_2 ETL was then spin coated from a 1:4 V/V diluted solution of the SnO_2 colloidal dispersion in fresh DI water using the spinning rate of 2000 rpm for 30 seconds. Before annealing, the coated electrode places were wiped off with cotton swabs dipped in DI water. The substrates were immediately transferred to the IPL machine to perform the annealing process using different flash counts having different energy quantities and were later put under a UV lamp to provide surface treatment and remove the organic contaminants for 15 min. The perovskite ink was then passed through a 0.45 μm PTFE syringe filter and spin-coated on the SnO_2 coated substrates at two consecutive spinning rates of 1000 rpm for 10 s and 3000 rpm for 30 s. During the last 12 s of the spinning

process, 200 μL of chlorobenzene solution was pipetted on the rotating substrate to take the solution to the supersaturation mode and form a transparent yellow wet film. The $Cs_{0.05}(MA_{0.85}FA_{0.15})_{0.95}PbI_3$ triple cation perovskite ink was made in a nitrogen filled glovebox in compliance to our previous ink engineering stated elsewhere [58]. In brief, 0.013 gr CsI, 0.6454 gr PbI_2, 0.0343 gr FAI, and 0.18 gr MAI was initially dissolved in 1 mL DMF and 0.125 mL DMSO. After complete dissolution and the formation of a transparent yellow solution, 0.25 mL di-iodomethane was pipetted to the solution and stirred for 2 hours to provide the complete dissolution. During the spinning process, a dry air stream was put in the spin coater chamber to keep the relative humidity less than 10%. After heating the wet perovskite film for 20 seconds on a hotplate at 110 °C, the slides were immediately taken to the IPL machine to perform rapid perovskite annealing through 5 pulses, each with 1.4 kJ energy. For flexible substrates, the wet film coated sheets were placed on a hotplate at 75 °C for 10 s to form a dark brown film and were subsequently sintered through a single IPL shot with 900 J energy, an optimal condition where perovskite film damage was observed at higher energy quantities. Both hotplate and IPL annealing steps were carried out in the ambient with relative humidity of 60%. Right after perovskite annealing, the substrates were transferred to a nitrogen filled glovebox for the Spiro-MeOTAD hole-transport layer deposition. The Spiro-MeOTAD solution was made by initially dissolving a 72.3 mg of Spiro-MeOTAD in 1mL chlorobenzene. 28.8 μL 4-*tert*-butyl-pyridine was then pipetted to the solution and mixed. Later, a 17.5 μL of a stock solution of 520 mg/mL lithium bis (trifluoromethylsulphonyl) imide in anhydrous acetonitrile was pipetted to the solution and stirred until full dissolution. Finally, 29 μL of the cobalt dopant FK209 TFSI salt (300 mg/mL in anhydrous acetonitrile) was pipetted to the mixture to prepare the final solution. The Spiro-MeOTAD film was made by spin-coating 70 μL of the prepared solution at 1700 rpm for 30 seconds. Ultimately, an 80 nm gold electrode was deposited through a thermal evaporator.

2.3. Characterization

XRD measurements were carried out within the 2θ range between 10° and 60° using a Bruker AXS D8 X-ray Diffractometer equipped with a position sensitive detector (PCD) and an X-ray source of CuKα (λ = 0.1548 nm) with the scanning speed of 1 Sec/Step and the step size of 0.02°. IPL annealing was done through a Xenon S-2000 rack-mounted sintering system with linear Xenon flash lamp placed within 5.7 cm from the substrates. Surface morphology inspections were done through a FEI Nova NanoSEM 600 SEM machine with an accelerating voltage of 10 kV and a working distance of 5 mm. The impedance spectroscopy (IS) and the current-voltage curves were obtained using an Autolab PGSTAT128-N potentiostat with the scanning rate of 0.1 V/Sec. Each cell was illuminated from the back side with an active area of 0.12 cm^2 using an AM 1.5 simulated light from a Newport LCS-100 solar simulator. The transmission and absorption spectra were obtained using PerkinElmer Lambda 950 UV−Vis spectrometer between 250 and 800 nm wavelengths. PL analysis was carried out using a Renishaw inVia Raman microscope with a CCD detector and a 632 nm He−Ne laser source. X-ray photoelectron spectroscopy (XPS) data was obtained from VG scientific MultiLab 3000 under ultrahigh vacuum pressure range within 10^{-8} Torr using an Mgkα radiation X-ray source (hν > 1253.6 eV) with respect to the carbon C1S peak position.

3. Results and discussion

In this study we have successfully fabricated planar n-i-p PSCs with ITO-PET and FTO-glass/SnO_2/Perovskite/Spiro-MeOTAD/gold thin film structure through a single step spin coating with rapid flash annealing from a xenon lamp on both SnO_2 ETL and the perovskite photoactive film under ambient conditions. We have previously shown that di-iodomethane (CH_2I_2) could improve the power conversion efficiency of $CH_3NH_3PbI_3$ solar cells by improving surface coverage, film morphology, and crystallinity of the perovskite material [58]. In this work, we, first, optimized the IPL annealing parameters for the diluted solution of the commercially available SnO_2 colloidal dispersion solution through four different IPL conditions, including 5 and 10 pulse counts, each with different light energies of 1.4 kJ and 2.1 kJ. Later, we incorporated di-iodomethane into the triple cation ($CH_3NH_3^+$, $(CH_3)_2NH_2^+$, Cs^+) perovskite precursor to determine how CH_2I_2 would interact with a different perovskite chemistry. Finally, the optimum conditions were picked to fabricate PSCs on both rigid and flexible substrates.

3.1. SnO_2 annealing optimization

To determine the surface coverage and film quality of SnO_2, SEM images of the FTO coated glass and SnO_2 coated thin films on glass-FTO substrates were taken and are shown in Fig. 1. The image of FTO, shown in Fig. 1(A), displays distinct grain boundaries under 200 nm magnification. In comparison, images of the SnO_2 film coated on glass-FTO, Fig. 1(B), appear granulated and the distinct grain boundaries shown in Fig. 1(A) are less apparent. This indicates that glass-FTO surface is covered with SnO_2, and the disappearance of grain boundaries determines successful uniform deposition of the SnO_2 film which should increase shunt resistances.

To understand the feasibility of IPL annealing on SnO_2 ETL, FTO glass slides carrying the wet spin coated SnO_2 film were immediately transferred to the IPL machine and different flash counts carrying various energy quantities were applied on them. During the pulse annealing process, the water content evaporates from the wet film and the SnO_2 nanoparticles are crystallized and become capable for charge carrier transportation. It is expected for the charge carrier transportation capability to be depended on the degree of SnO_2 crystallization which, in turn, is depended on the heat flux per flash, as well as the duration and count of the flashes. Due to the limitation of our IPL machine being capable to provide 2 ms duration flashes, we only studied the crystallization through variation of the flash energy and counts. The applied pulse energies were 1.4 kJ and 2.1 kJ, and four different pulse counts of 1, 3, 5, 10, and 15 were selected for each pulse energy to anneal the SnO_2 film.

To study the chemical state, XPS was employed to probe the surface of our IPL annealed SnO_2 thin films and is highlighted in Fig. 2. Fig. 2(A) indicates the full XPS spectrum of the SnO_2 thin film fabricated through the optimal annealing condition of 5 pulses at 2.1 kJ energy, and the XPS patterns for 5 pulses at 1.4 kJ, 10 pulses at 1.4 kJ, and 10 pulses at 2.1 kJ conditions are included in Fig. S1 of the supplementary data. It can be clearly observed that all XPS graphs indicated a neat pattern demonstrating intense peaks of Sn and O without any other chemical species and functional groups which can suggest the formation of uncontaminated samples containing high concentration of Sn and O elements. The two small peaks at 293 and 295.5 eV are attributed to $K2P_{3/2}$ and $K2P_{1/2}$ orbitals of potassium ions used as the stabilizer in making the commercial product of the SnO_2 colloidal dispersion solution [59]. We assume that the bonding nature of surface level Sn−O observed in XPS spectra will be indicative of the bulk material given that the film is about 25−40 nm thick. The O1s peak can be deconstructed into two components indicative of $O-Sn^{4+}$ and $O-Sn^{2+}$, as shown in Fig. 2(B) [60]. The $O-Sn^{4+}$ peak is higher in binding energy than the $O-Sn^{2+}$ peak; hence, the IPL processing condition that maximizes the O1s binding energy will maximize the surface concentration of SnO_2. The O1S peak intensity for all the IPL annealing conditions remained similar which can be an indicator of unchanged oxygen

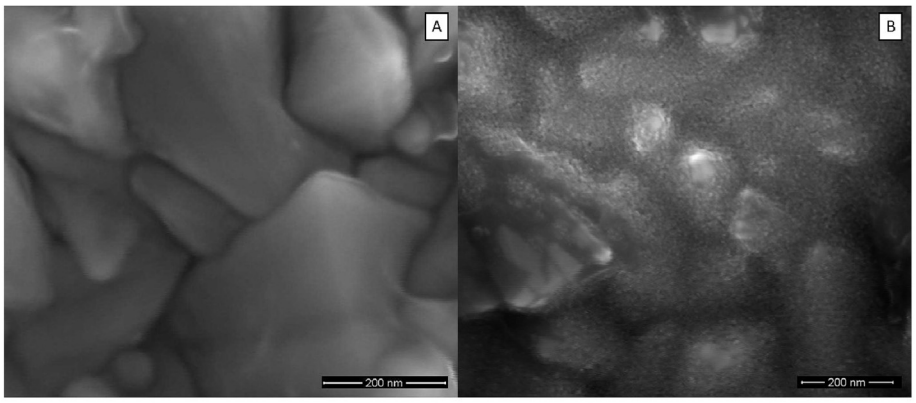

Fig. 1:. Top surface SEM images of (A) FTO film on glass; and (B) SnO_2 film on FTO showing SnO_2 coverage.

concentration change. However, the binding energy of O1s peak was maximized when processed through 5 pulses at 2.1 kJ IPL condition, which can indicate enhanced Sn–O interaction and, thus, strengthened bonding that can better facilitate charge carrier transportation. Similar to O1s peak, the $3d_{5/2}$ peak is a combination of the Sn^{4+} and Sn^{2+} oxidation states [60]. The Sn^{2+} oxidation state arises from oxygen vacancies formed during the spin-coating process and is lower in binding energy than the Sn^{4+} oxidation state [61]. The presence of Sn^{4+} oxidation state indicates SnO_2 formation; therefore, the IPL processing condition that maximizes the binding energy of Sn $3d_{5/2}$ peak is the optimal SnO_2 processing condition. Fig. 2(C) shows that the binding energy of Sn $3d_{5/2}$ peak is maximized for SnO_2 thin films processed through 5 pulses at 2.1 kJ with respect to other processing conditions, which, in addition to the obtained results from O1S peak, suggests that this condition would yield the optimal crystallization of the deposited SnO_2 films and is consistent with other reports [62]. The peak intensity for all IPL conditions were almost identical, suggesting that the relative change in Sn concentration was insignificant. Table 1 contains Sn and O core level binding energies from the XPS surveys for each of the SnO_2 films annealed through different IPL conditions.

It is noteworthy that determining the crystallinity using XRD was attempted; however, the results did not reveal any peaks due to the film being extremely thin. Therefore, XPS was used to demonstrate a response of the material at different IPL processing

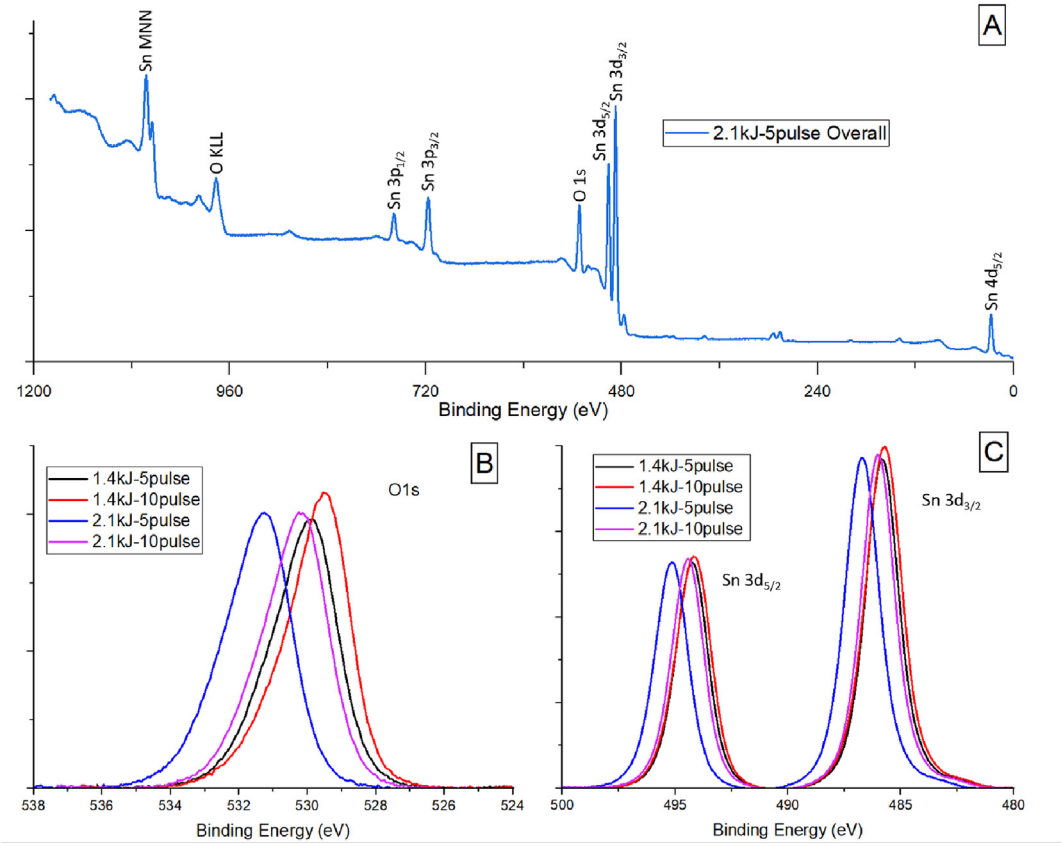

Fig. 2. A) XPS survey of the SnO_2 ETL annealed through 5 pulses at 2.1 kJ IPL condition; XPS patterns of B) O1S; and C) Sn state of the SnO_2 ETL sintered at various IPL conditions.

Table 1
Core level binding energy data for Sn and O after different IPL annealing conditions.

IPL condition	$Sn3d_{5/2}$ Binding Energy (eV)	$Sn3d_{3/2}$ Binding Energy (eV)	O1s Binding Energy (eV)
1.4 kJ_5 Pulse	494.25	485.85	529.85
1.4 kJ_10 Pulse	494.20	485.70	529.55
2.1 kJ_5 Pulse	495.15	486.70	531.25
2.1 kJ_10 Pulse	494.45	486.00	530.25

parameters.

Fig. 3(A) displays the Tauc plot, photon energy versus $(\alpha h\nu)^2$, of SnO_2 which is used to measure the bandgap of the material. As it is apparent, SnO_2 thin films annealed through 5 pulses at 1.4 kJ and 2.1 kJ IPL conditions had the lowest and highest bandgap of 3.72 eV and 3.74 eV, respectively.

Fig. 3(B) shows the PL spectra for SnO_2 thin films annealed through different IPL conditions. The peak intensity was minimized when SnO_2 films were fabricated through 5 pulses at 2.1 kJ IPL condition. A reduction in PL intensity indicates less charge recombination at the SnO_2/perovskite interface [63]. Therefore, it can be suggested that the annealing of film through 5 pulses at 2.1 kJ condition would yield the maximum charge transport in comparison to the other annealing conditions. In addition, it can be observed that the PL peaks were slightly shifted for the SnO_2 films annealed through different IPL conditions, demonstrating a blue shift behavior for the films annealed through flashes carrying higher heat fluxes. This blueshift is in accordance with ~ 0.02 eV bandgap difference shown in Fig. 3(A) which can indicate diminished trap emissions and, thus, stronger exciton emissions at elevated flash heat fluxes and conforms with other reports [64,65].

We further studied the interfacial and in-layer charge transportation of IPL processed PSCs through impedance spectroscopy (IS) as shown in Fig. 4. Operating at open-circuit voltage under low light intensity has been shown to isolate the hole accumulation zone built up between perovskite absorber and ETL [66,67]. A reduction in overall impedance of the PSCs at open-circuit voltage indicates that charge carriers were more efficiently extracted from the perovskite absorber layer. The impedance was minimized for PSCs, in which, the SnO_2 layer was annealed through 5 pulses at 2.1 kJ condition. These results are consistent with the PL data shown in Fig. 3(B) and suggest that annealing through 5 pulses at 2.1 kJ would be the optimum IPL condition. Further study on material characteristics of the low temperature annealed SnO_2 films obtained from the commercial colloidal dispersion is provided in our other work [68].

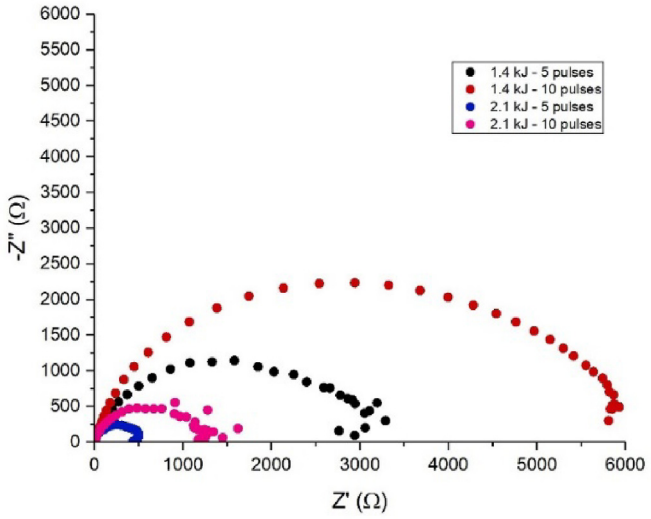

Fig. 4. Impedance spectra of PSCs at four different IPL conditions on SnO_2.

3.2. Perovskite optimization

Alkyl-halide additives improve solvent-precursor interactions, allowing for higher perovskite film quality and better surface coverage. In our previous study, we added CH_2I_2 to $CH_3NH_3PbI_3$ perovskite precursor solution and observed improvements in power conversion efficiency, surface coverage, and film morphology [58]. Herein, we incorporated CH_2I_2 into the triple cation perovskite precursor solution to investigate the possible performance improvement of PSCs after introducing CH_2I_2 into a new perovskite chemistry. To discern whether CH_2I_2 improved the perovskite film quality and surface coverage, top-down SEM images of the annealed perovskite film, with and without CH_2I_2 after IPL annealing, is shown in Fig. 5. Fig. 5(A) suggests that a fine

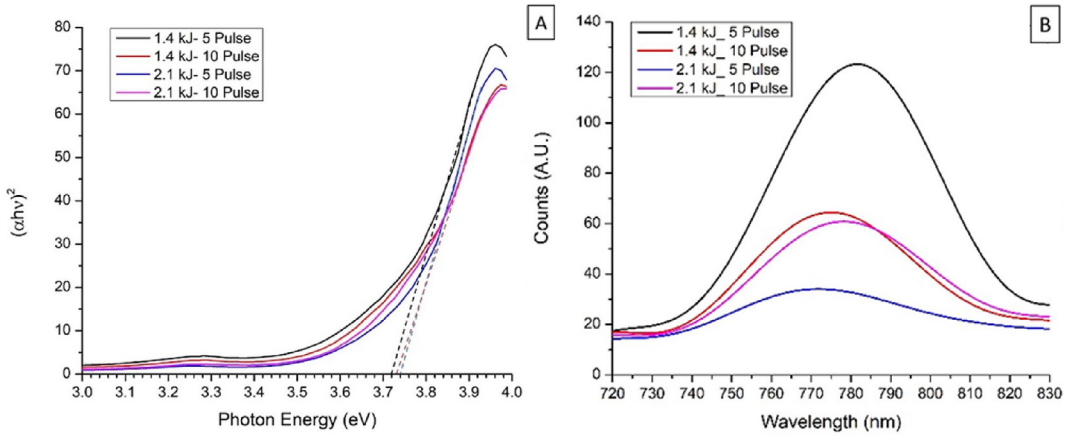

Fig. 3. A) Tauc's plot demonstrating SnO_2 bandgap at various IPL conditions; and B) PL spectra of SnO_2 films annealed through different IPL conditions with FTO/SnO_2/perovskite structure.

perovskite film without observable pinholes was formed when CH_2I_2 was incorporated into the precursor solution. In comparison, Fig. 5(B) contains a top-down SEM image of IPL annealed perovskite without the diiodomethane additive. The image indicates the formation of smaller grain sizes with dendrite structures within the perovskite film, indicating natural crystallization within the wet film prior to the annealing process. Formation of dendrite structures can reduce the quality of thin film, while smaller grain sizes can enhance charge recombination at the grain boundaries due to the formation of more grain boundary density within the film, thus, decreasing the photovoltaic performance. To find out the average grain sizes, ImageJ was used to obtain the size and area of individual grains within the captured top surface SEM image of the perovskite films after IPL annealing. The results indicated average crystal size and area of 201 nm, and 0.031 μm^2 for the CH_2I_2 containing perovskite films, and 138 nm, and 0.015 μm^2 for the films made from pristine solution, delineating almost 1.45 times crystal growth for the devices made with aid of di-iodomethane additive. The histograms of grain size and area are included in Fig. S2 of the supplementary data. The SEM images suggest that CH_2I_2 additive improved surface coverage, grain growth, and film quality of the triple cation perovskite layer by implementing two significant roles. First, the addition of diiodomethane could potentially increase the solution boiling point and delay the unfavorable natural crystallization of the as-spinning solution, thus, hindering the inadequate crystallization of the film and insufficient grain growth upon annealing. Second, CH_2I_2 could improve the crystallinity of perovskite layer due to its role as an iodide source. When exposed to IPL, the C—I bond is broken, yielding equal parts CH_2I^+ and I^-. The I^- ions are then incorporated into the perovskite material by filling iodine vacancies [58]. The released iodine from alkyl halide could replace the lost iodine through evaporation during the annealing processes, thus avoiding the formation of defected perovskite black phase upon the completion of annealing. Therefore, it is expected that di-iodomethane addition would improve the device performance through enhanced charge carrier production and extraction to the transport films, thus decreasing and increasing the series and shunt resistances, respectively. Crystallization kinetics, surface coverage, and improved crystallinity are all examples of how the CH_2I_2 additive, in cooperation with IPL, can improve the quality of the perovskite absorber layer.

Fig. 5(C) shows the absorbance spectra for the FTO/SnO_2/perovskite and FTO/SnO_2 structures after optimum IPL annealing. Similar to our previous work for $CH_3NH_3PbI_3$ photoactive films, the triple cation perovskite films were brown in color after short-term hotplate annealing and became darker after IPL annealing, thus, becoming capable of efficiently absorbing the light energy. The FTO/SnO_2/perovskite structure demonstrated high absorption within 400−750 nm wavelengths range; whereas, the FTO/SnO_2 structure possessed little to no absorption within 400−800 nm range. This indicates that the full AM1.5 spectrum reaches the perovskite absorber without being consumed by the ETL. The final device will be constructed in a manner where light travels through glass, FTO, SnO_2, then strikes perovskite where it can be absorbed.

XRD patterns shown in Fig. 2(D) reveal information about crystallinity of the perovskite layer after IPL annealing. The intense 2θ peaks around 26.5°, 33.75°, 37.5°, 51.2°, and 54.5° are indicative of FTO/SnO_2, and the strong peaks around 14.06°, 20°, 24.4°, 28.4°, 31.8°, 34.9°, 40.5°, 43°, and 50.5° are associated to (110), (112), (202), (220), (310), (312), (224), (314), and (404) crystal planes which indicates the formation of perovskite tetragonal black phase. The perovskite tetragonal black phase is the preferred conformation for PSCs. Fortunately, the patterns did not reveal the PbI_2 peak around 12.4° which indicated the complete formation of a pure perovskite black phase. Formation of a pure perovskite black phase would promote higher PSC efficiency due to fewer series and higher

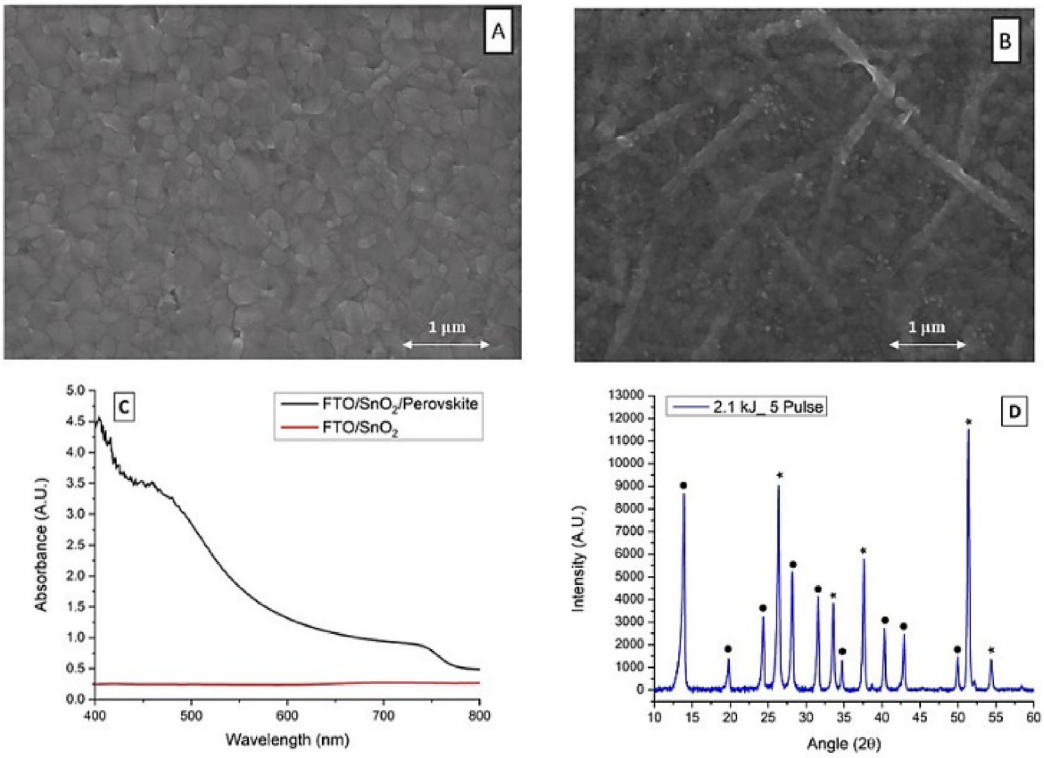

Fig. 5. Top surface SEM image of the IPL annealed perovskite layer through 5 pulses at 1.4 kJ energy with A) CH_2I_2 additive; and B) without CH_2I_2 additive deposited on SnO_2 thin film annealed through 5 pulses at 2.1 kJ IPL condition; C) Absorbance spectra of the FTO/SnO_2/perovskite and FTO/SnO_2 structures after optimum IPL annealing; and D) XRD pattern of the FTO/SnO_2/perovskite structure demonstrating FTO/SnO_2 (*) and perovskite (•) peaks after IPL annealing.

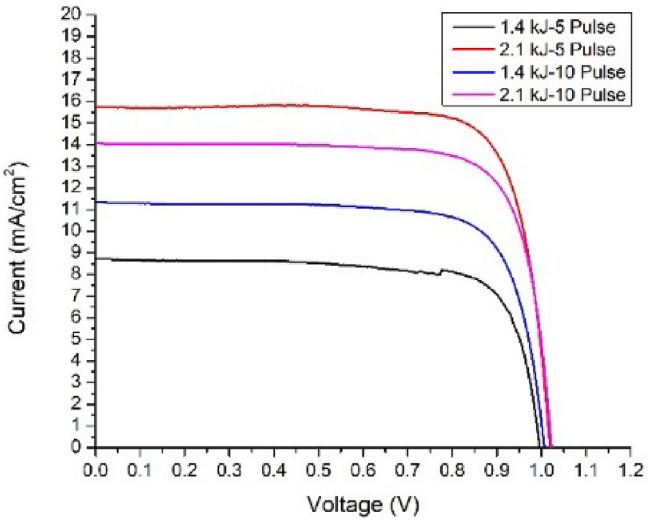

Fig. 6. J-V performance data of PSCs fabricated using four different IPL conditions on the SnO_2 layer.

3.3. Device performance

To verify the observed characterization results, we finally fabricated PSCs to measure the device functionality. The overall performance summary of PSCs fabricated using four different IPL conditions on SnO_2 ETL is shown in Table 2, and the current density-voltage (J-V) curve of champion cell for each IPL condition is shown in Fig. 6. The results indicate that exposing the SnO_2 thin films to higher pulse energy flux of 2.1 kJ can provide better device performance than the lower pulse energy of 1.4 kJ for all the range of applied pulse counts, which implies the significance of heat flux intensity on material crystallization. On the other hand, lower pulse counts for the higher pulse energy were found to provide the maximum device performance, determining the 5 pulse at 2.1 kJ as the optimal IPL annealing condition which could result in the highest device performance. As shown by the results, varying the IPL annealing conditions for SnO_2 ETL could considerably affect the current flow throughout the fabricated cells while maintaining the voltage and fill factor. This observation can indicate the significance of IPL annealing conditions on the crystallization of the metal oxide material which play a vital role on facilitating charge extraction at the thin film interface and throughout the film. It was found after several experiments that pulse counts higher than 10 could not enhance the current flow, while pulse counts lower than five resulted in dead cells, demonstrating a resistor behavior. This is consistent with the XRD pattern of unannealed drop casted SnO_2 shown in Fig. S3 of the supplementary data which demonstrated broad peaks with low intensity and, hence, its amorphous nature.

Table 2
Overall performance summary of PSCs in which SnO_2 thin films were fabricated through four different IPL conditions (5 cells for each condition).

IPL conditions	Diiodomethane	J_{sc}(mA/cm^2)	V_{oc}(V)	FF (%)	PCE (%)
1.4 kJ- 5 pulse	Yes	11.80 ± 0.60	0.92 ± 0.045	67.40 ± 3.71	6.78 ± 0.39
1.4 kJ- 10 pulse	Yes	12.67 ± 0.56	0.976 ± 0.019	74.98 ± 0.49	9.27 ± 0.49
2.1 kJ- 5 pulse	Yes	15.84 ± 0.54	0.995 ± 0.014	76.3 ± 1.28	11.98 ± 0.35
2.1 kJ-10 pulse	Yes	14.22 ± 0.11	0.989 ± 0.015	67.78 ± 6.18	9.56 ± 0.98
2.1 kJ- 5 pulse	No	14.95 ± 0	0.811 ± 0.024	53.8 ± 2.16	6.38 ± 0.74

recombination resistances within the perovskite absorber layer. Therefore, the applied IPL annealing condition for the perovskite film could sufficiently crystallize the layer without causing post degradation of the film nor being insufficient to leave the perovskite yellow phase unconverted to black phase.

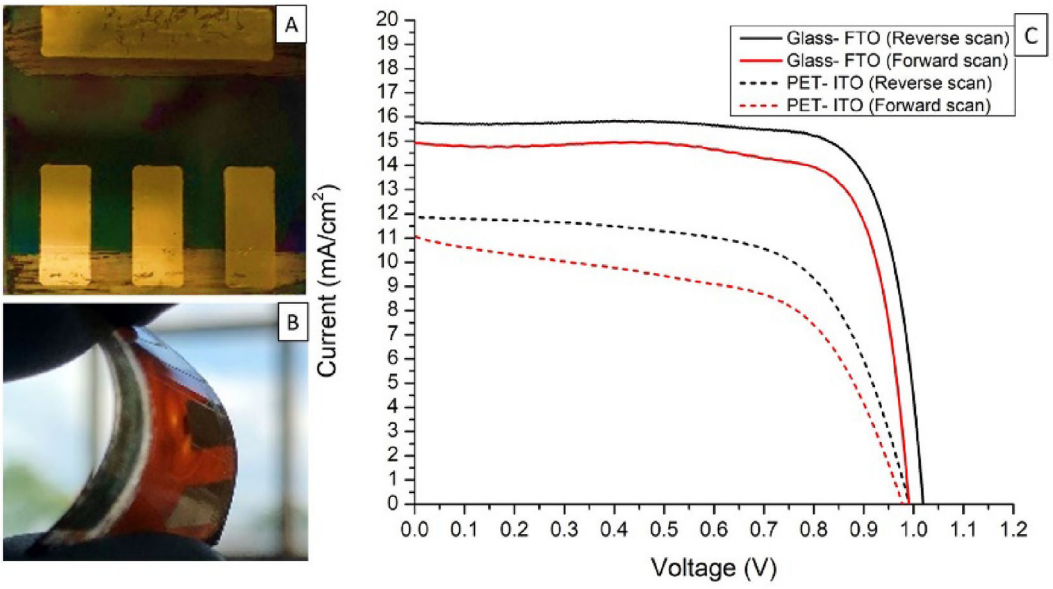

Fig. 7. Illustration of the fabricated PSC on A) rigid glass-FTO; and B) PET-ITO flexible substrates. C) Reverse and forward J-V characteristics of the champion rigid and flexible PSCs.

Therefore, thermal annealing is required to crystallize the material and there is an existing optimal annealing condition, in which, exceeding the limit would not result in an operative or economical fabrication of device. It is noteworthy that providing pulse energies higher than 2.1 kJ were not possible due to the limitation of our current annealing machine. Perhaps higher pulses than the studied conditions followed by lower pulse counts can result in further enhanced device performance. Further study over IPL annealing conditions on PSCs thin film morphology and device efficiency will be discussed in the future works. In this interim, we have provided the photovoltaic parameters and conducted the study over the impact of IPL annealing on SnO_2 structure only for the IPL annealing conditions within the range of functional devices.

3.4. Flexible PSCs

To further investigate the scalability of rapid thermal annealing through IPL on both SnO_2 and perovskite thin films, we also fabricated PSCs on roll-to-roll favorable flexible PET-ITO substrates. Fig. 7 shows the J-V characteristics of the forward and reverse scan of champion rigid and flexible substrates annealed through the optimum SnO_2 IPL annealing condition of 5 pulses at 2.1 kJ. The J-V characteristics of rigid and flexible PSCs indicated the maximum reverse scan efficiency of 12.56% and 7.6%, open circuit voltage (V_{oc}) of 1.02 and 0.993 V, short-circuit current density (J_{SC}) of 15.78 and 11.87 mA/cm^2, and the fill factor of 78.3% and 64.75%, as well as the maximum forward scan efficiency of 11.33% and 6.16%, V_{oc} of 0.992 and 0.979 V, short-circuit current density of 14.92 and 11.06 mA/cm^2, and the fill factor of 76.7% and 56.95%, demonstrating relatively low J-V hysteresis for both rigid and flexible PSCs. It can be observed from the experimental results that the flexible PSCs had a lower performance compared to rigid cells. This lack of performance can be attributed to the higher resistance of ITO coated sheets compared to FTO slides, handling of the flexible substrates during fabrication processes, as well as unsuitable nature of spin-coating method to form highly uniform films with superior quality, particularly for coating water based SnO_2 films on smooth ITO coated sheets compared to rough FTO substrates, which require the application of actual roll-to-roll fabrication setup and will be addressed in future works. Our results delineated that CH_2I_2 additive is also applicable for another perovskite chemistry and its synergy with sequential step IPL annealing is a potential candidate for rapid and economical industrial scale manufacturing of PSCs on both the rigid and roll-to-roll favorable flexible substrates.

4. Conclusion

In this study, fabrication of PSCs through intense flashed annealing was demonstrated for both the SnO_2 electron transport layer (ETL) and di-iodomethane (CH_2I_2) assisted $Cs_{0.05}(MA_{0.85}FA_{0.15})_{0.95}PbI_3$ mixed triple cation perovskite thin films both on rigid glass-FTO and flexible PET-ITO substrates. It was shown that the addition of CH_2I_2 could eliminate natural perovskite crystallization by increasing the precursor ink boiling point and form a superior dry film morphology with bound grains as a result of iodine release during the annealing processes. This resulted in PSCs with efficiency and fill factors as high as 12.56% and 78.3% for rigid FTO-glass substrates, and 7.6% and 64.75% for flexible ITO-PET sheets, when the SnO_2 ETL was optimally annealed through 5 pulses of IPL, each carrying 2.1 kJ energy. It was shown that sequential step IPL annealing can be used for rapid fabrication of PSCs and eliminate the need for prolonged annealing of the charge carrier and photoactive thin films. Our results demonstrated the possibility of obtaining efficient cells with high fill factor through IPL annealing from a single-step spin-coating for various PSC thin films without the application of any dopants or surface treatments. To our knowledge, this work provided the fastest route of fabricating PSCs so far, and is the first reported manuscript on rapid thermal annealing of the SnO_2 ETL and di-iodomethane assisted triple cation perovskite absorber films within seconds of time frame cumulatively, which can provide the possibility of a swift and cost-effective fabrication of PSCs through roll to roll.

Data availability

The datasets generated and/or analyzed during the current study are available from the corresponding author on reasonable request.

CRediT authorship contribution statement

Amir H. Ghahremani: Conceptualization, Formal analysis, Writing - original draft, Writing - review & editing. **Blake Martin:** Conceptualization, Formal analysis, Writing - original draft, Writing - review & editing. **Alexander Gupta:** Conceptualization, Formal analysis, Writing - original draft, Writing - review & editing. **Jitendra Bahadur:** Conceptualization, Formal analysis, Writing - original draft, Writing - review & editing. **Krishnamraju Ankireddy:** Conceptualization, Formal analysis, Writing - original draft, Writing - review & editing. **Thad Druffel:** Conceptualization, Formal analysis, Writing - original draft, Writing - review & editing.

Acknowledgement

The authors knowledge the Conn center for renewable energy research at the University of Louisville for their financial support and research facilities.

Appendix A. Supplementary data

Supplementary data to this article can be found online at https://doi.org/10.1016/j.matdes.2019.108237.

References

[1] Y.H. Park, I. Jeong, S. Bae, H.J. Son, P. Lee, J. Lee, C.H. Lee, M.J. Ko, Inorganic rubidium cation as an enhancer for photovoltaic performance and moisture stability of HC(NH2)2PbI3 perovskite solar cells, Adv. Funct. Mater. 27 (2017), 1605988, https://doi.org/10.1002/adfm.201605988.
[2] T. Singh, T. Miyasaka, High performance perovskite solar cell via multi-cycle low temperature processing of lead acetate precursor solutions, Chem. Commun. 52 (2016) 4784–4787, https://doi.org/10.1039/C5CC10608G.
[3] A. Kojima, K. Teshima, Y. Shirai, T. Miyasaka, Organometal halide perovskites as visible-light sensitizers for photovoltaic cells, J. Am. Chem. Soc. 131 (2009) 6050–6051, https://doi.org/10.1021/ja809598r.
[4] https://www.nrel.gov/pv/cell-efficiency.html.
[5] M.R. Filip, G.E. Eperon, H.J. Snaith, F. Giustino, Steric engineering of metal-halide perovskites with tunable optical band gaps, Nat. Commun. 5 (2014) 5757, https://doi.org/10.1038/ncomms6757.
[6] F. Hao, C.C. Stoumpos, D.H. Cao, R.P.H. Chang, M.G. Kanatzidis, Lead-free solid-state organic-inorganic halide perovskite solar cells, Nat. Photonics 8 (2014) 489–494, https://doi.org/10.1038/nphoton.2014.82.
[7] C.S. Ponseca Jr., T.J. Savenije, M. Abdellah, K. Zheng, A. Yartsev, T.r. Pascher, T. Harlang, P. Chabera, T. Pullerits, A. Stepanov, Organometal halide perovskite solar cell materials rationalized: ultrafast charge generation, high and microsecond-long balanced mobilities, and slow recombination, J. Am. Chem. Soc. 136 (2014) 5189–5192, https://doi.org/10.1021/ja412583t.
[8] Q. Dong, Y. Fang, Y. Shao, P. Mulligan, J. Qiu, L. Cao, J. Huang, Electron-hole diffusion lengths>175 um in solution-grown CH3NH3PbI3 single crystals, Science 347 (2015) 967–970, https://doi.org/10.1126/science.aaa5760.
[9] Z. Yang, A. Surrente, K. Galkowski, N. Bruyant, D.K. Maude, A.A. Haghighirad, H.J. Snaith, P. Plochocka, R.J. Nicholas, Unraveling the exciton binding energy and the dielectric constant in single-crystal methylammonium lead triiodide perovskite, J. Phys. Chem. Lett. 8 (2017) 1851–1855, https://doi.org/10.1021/acs.jpclett.7b00524.
[10] S. De Wolf, J. Holovsky, S.-J. Moon, P. Loper, B. Niesen, M. Ledinsky, F.-J. Haug, J.-H. Yum, C. Ballif, Organometallic halide perovskites: sharp optical absorption edge and its relation to photovoltaic performance, J. Phys. Chem. Lett. 5 (2014) 1035–1039, https://doi.org/10.1021/jz500279b.
[11] Z. Xiao, Y. Yuan, Q. Wang, Y. Shao, Y. Bai, Y. Deng, Q. Dong, M. Hu, C. Bi,

J. Huang, Thin-film semiconductor perspective of organometal trihalide perovskite materials for high-efficiency solar cells, Mater. Sci. Eng. R Rep. 101 (2016) 1–38, https://doi.org/10.1016/j.mser.2015.12.002.
[12] N.J. Jeon, J.H. Noh, W.S. Yang, Y.C. Kim, S. Ryu, J. Seo, S.I. Seok, Compositional engineering of perovskite materials for high-performance solar cells, Nature 517 (2015) 476–480, https://doi.org/10.1038/nature14133.
[13] K.L. Gardner, J.G. Tait, T. Merckx, W. Qiu, U.W. Paetzold, L. Kootstra, M. Jaysankar, R. Gehlhaar, D. Cheyns, P. Heremans, Nonhazardous solvent systems for processing perovskite photovoltaics, Adv. Energy Mater. 6 (2016) 1600386, https://doi.org/10.1002/aenm.201600386.
[14] M. Habibi, A. Rahimzadeh, I. Bennouna, M. Eslamian, Defect-free large-area (25 cm2) light absorbing perovskite thin films made by spray coating, Coatings 7 (2017) 42, https://doi.org/10.3390/coatings7030042.
[15] C.F.J. Lau, X. Deng, Q. Ma, J. Zheng, J.S. Yun, M.A. Green, S. Huang, A.W.Y. Ho-Baillie, CsPbIBr2 perovskite solar cell by spray-assisted deposition, ACS Energy Lett. 1 (2016) 573–577, https://doi.org/10.1021/acsenergylett.6b00341.
[16] D.-H. Lan, S.-H. Hong, L.-H. Chou, X.-F. Wang, C.-L. Liu, High throughput two-step ultrasonic spray deposited CH 3 NH 3 PbI 3 thin film layer for solar cell application, J. Power Sources 390 (2018) 270–277, https://doi.org/10.1016/j.jpowsour.2018.04.031.
[17] L.-H. Chou, X.-F. Wang, I. Osaka, C.-G. Wu, C.-L. Liu, Scalable ultrasonic spray-processing technique for manufacturing large-area CH3NH3PbI3 perovskite solar cells, ACS Appl. Mater. Interfaces 10 (2018) 38042–38050, https://doi.org/10.1021/acsami.8b12463.
[18] E. Perez-Gutierrez, J. Lozano, J. Gaspar-Tanori, J.-L. Maldonado, B. Gomez, L. Lopez, L.-F. Amores-Tapia, O. Barbosa-Garcia, M.-J. Percino, Organic solar cells all made by blade and slot-die coating techniques, Sol. Energy 146 (2017) 79–84, https://doi.org/10.1016/j.solener.2017.02.004.
[19] Y. Galagan, F. Di Giacomo, H. Gorter, G. Kirchner, I. de Vries, R. Andriessen, P. Groen, Roll-to-Roll slot die coated perovskite for efficient flexible solar cells, Adv. Energy Mater. 8 (2018) 1801935, https://doi.org/10.1002/aenm.201801935.
[20] B. Dou, J.B. Whitaker, K. Bruening, D.T. Moore, L.M. Wheeler, J. Ryter, N.J. Breslin, J.J. Berry, S.M. Garner, F.S. Barnes, Roll-to-Roll printing of perovskite solar cells, ACS Energy Lett. 3 (2018) 2558–2565, https://doi.org/10.1021/acsenergylett.8b01556.
[21] F. Di Giacomo, S. Shanmugam, H. Fledderus, B.J. Bruijnaers, W.J. Verhees, M.S. Dorenkamper, S.C. Veenstra, W. Qiu, R. Gehlhaar, T. Merckx, Up-scalable sheet-to-sheet production of high efficiency perovskite module and solar cells on 6-in. substrate using slot die coating, Sol. Energy Mater. Sol. Cells 181 (2018) 53–59, https://doi.org/10.1016/j.solmat.2017.11.010.
[22] A.T. Mallajosyula, K. Fernando, S. Bhatt, A. Singh, B.W. Alphenaar, J.-C. Blancon, W. Nie, G. Gupta, A.D. Mohite, Large-area hysteresis-free perovskite solar cells via temperature controlled doctor blading under ambient environment, Appl. Mater. Today 3 (2016) 96–102, https://doi.org/10.1016/j.apmt.2016.03.002.
[23] Q. Hu, H. Wu, J. Sun, D. Yan, Y. Gao, J. Yang, Large-area perovskite nanowire arrays fabricated by large-scale roll-to-roll micro-gravure printing and doctor blading, Nanoscale 8 (2016) 5350–5357, https://doi.org/10.1039/C5NR08277C.
[24] C. Zhang, Q. Luo, H. Wu, H. Li, J. Lai, G. Ji, L. Yan, X. Wang, D. Zhang, J. Lin, Roll-to-roll micro-gravure printed large-area zinc oxide thin film as the electron transport layer for solution-processed polymer solar cells, Org. Electron. 45 (2017) 190–197, https://doi.org/10.1016/j.orgel.2017.03.015.
[25] Z. Wei, H. Chen, K. Yan, S. Yang, Inkjet printing and instant chemical transformation of a CH3NH3PbI3/nanocarbon electrode and interface for planar perovskite solar cells, Angew. Chem. 126 (2014) 13455–13459, https://doi.org/10.1002/anie.201408638.
[26] P. Li, C. Liang, B. Bao, Y. Li, X. Hu, Y. Wang, Y. Zhang, F. Li, G. Shao, Y. Song, Inkjet manipulated homogeneous large size perovskite grains for efficient and large-area perovskite solar cells, Nano Energy 46 (2018) 203–211, https://doi.org/10.1016/j.nanoen.2018.01.049.
[27] A.J. Huckaba, Y. Lee, R. Xia, S. Paek, V.C. Bassetto, E. Oveisi, A. Lesch, S. Kinge, P.J. Dyson, H. Girault, Inkjet-printed mesoporous TiO2 and perovskite layers for high efficiency perovskite solar cells, Energy Technol. 7 (2019) 317–324, https://doi.org/10.1002/ente.201800905.
[28] G.E. Eperon, V.M. Burlakov, P. Docampo, A. Goriely, H.J. Snaith, Morphological control for high performance, solution-processed planar heterojunction perovskite solar cells, Adv. Funct. Mater. 24 (2014) 151–157, https://doi.org/10.1002/adfm.201302090.
[29] Y. Liu, I. Shin, I.-W. Hwang, J. Lee, S. Kim, D.Y. Lee, S.-H. Lee, J.-W. Jang, Y.K. Jung, J.H. Jeong, Effective hot-air annealing for improving the performance of perovskite solar cells, Sol. Energy 146 (2017) 359–367, https://doi.org/10.1016/j.solener.2017.03.005.
[30] J. Troughton, C.c. Charbonneau, M.J. Carnie, M.L. Davies, D.A. Worsley, T.M. Watson, Rapid processing of perovskite solar cells in under 2.5 seconds, J. Mater. Chem. 3 (2015) 9123–9127, https://doi.org/10.1039/C5TA00568J.
[31] H.-S. Ko, J.-W. Lee, N.-G. Park, 15.76% efficiency perovskite solar cells prepared under high relative humidity: importance of PbI 2 morphology in two-step deposition of CH 3 NH 3 PbI 3, J. Mater. Chem. 3 (2015) 8808–8815, https://doi.org/10.1039/C5TA00658A.
[32] J.W. Jung, S.T. Williams, A.K.Y. Jen, Low-temperature processed high-performance flexible perovskite solar cells via rationally optimized solvent washing treatments, RSC Adv. 4 (2014) 62971–62977, https://doi.org/10.1039/C4RA13212B.
[33] M. Zhang, J.S. Yun, Q. Ma, J. Zheng, C.F.J. Lau, X. Deng, J. Kim, D. Kim, J. Seidel, M.A. Green, High-efficiency rubidium-incorporated perovskite solar cells by gas quenching, ACS Energy Lett. 2 (2017) 438–444, https://doi.org/10.1021/acsenergylett.6b00697.
[34] X. Li, D. Bi, C. Yi, J.-D. Decoppet, J. Luo, S.M. Zakeeruddin, A. Hagfeldt, M. Gratzel, A vacuum flash-assisted solution process for high-efficiency large-area perovskite solar cells, Science 353 (2016) 58–62, https://doi.org/10.1126/science.aaf8060.
[35] J. Chen, J. Xu, L. Xiao, B. Zhang, S. Dai, J. Yao, Mixed-organic-cation (FA) x (MA) 1-x PbI3 planar perovskite solar cells with 16.48% efficiency via a low-pressure vapor-assisted solution process, ACS Appl. Mater. Interfaces 9 (2017) 2449–2458, https://doi.org/10.1021/acsami.6b13410.
[36] X. Xia, W. Wu, H. Li, B. Zheng, Y. Xue, J. Xu, D. Zhang, C. Gao, X. Liu, Spray reaction prepared FA 1-x Cs x PbI 3 solid solution as a light harvester for perovskite solar cells with improved humidity stability, RSC Adv. 6 (2016) 14792–14798, https://doi.org/10.1039/C5RA23359C.
[37] T.P. Gujar, M. Thelakkat, Highly reproducible and efficient perovskite solar cells with extraordinary stability from robust CH3NH3PbI3: towards large-area devices, Energy Technol. 4 (2016) 449–457, https://doi.org/10.1002/ente.201500421.
[38] B. Conings, J. Drijkoningen, N. Gauquelin, A. Babayigit, J. D'Haen, L. D'Olieslaeger, A. Ethirajan, J. Verbeeck, J. Manca, E. Mosconi, Intrinsic thermal instability of methylammonium lead trihalide perovskite, Adv. Energy Mater. 5 (2015) 1500477, https://doi.org/10.1002/aenm.201500477.
[39] S. Collavini, M. Saliba, W.R. Tress, P.J. Holzhey, S.F. Völker, K. Domanski, S.H. Turren-Cruz, A. Ummadisingu, S.M. Zakeeruddin, A. Hagfeldt, Poly (ethylene glycol)–[60] fullerene-based materials for perovskite solar cells with improved moisture resistance and reduced hysteresis, ChemSusChem 11 (2018) 1032–1039, https://doi.org/10.1002/cssc.201702265.
[40] J. Bahadur, A.H. Ghahremani, S. Gupta, T. Druffel, M.K. Sunkara, K. Pal, Enhanced moisture stability of MAPbI3 perovskite solar cells through Barium doping, Sol. Energy 190 (2019) 396–404, https://doi.org/10.1016/j.solener.2019.08.033.
[41] C. Liu, W. Ding, X. Zhou, J. Gao, C. Cheng, X. Zhao, B. Xu, Efficient and stable perovskite solar cells prepared in ambient air based on surface-modified perovskite layer, J. Phys. Chem. C 121 (2017) 6546–6553, https://doi.org/10.1021/acs.jpcc.7b00847.
[42] H.-S. Rao, B.-X. Chen, W.-G. Li, Y.-F. Xu, H.-Y. Chen, D.-B. Kuang, C.-Y. Su, Improving the extraction of photogenerated electrons with SnO2 nanocolloids for efficient planar perovskite solar cells, Adv. Funct. Mater. 25 (2015) 7200–7207, https://doi.org/10.1002/adfm.201501264.
[43] Q. Jiang, L. Zhang, H. Wang, X. Yang, J. Meng, H. Liu, Z. Yin, J. Wu, X. Zhang, J. You, Enhanced electron extraction using SnO 2 for high-efficiency planar-structure HC (NH 2) 2 PbI 3-based perovskite solar cells, Nature Energy 2 (2017) 16177, https://doi.org/10.1038/nenergy.2016.177.
[44] Y. Lee, S. Paek, K.T. Cho, E. Oveisi, P. Gao, S. Lee, J.-S. Park, Y. Zhang, R. Humphry-Baker, A.M. Asiri, Enhanced charge collection with passivation of the tin oxide layer in planar perovskite solar cells, J. Mater. Chem. 5 (2017) 12729–12734, https://doi.org/10.1039/C7TA04128D.
[45] Y.C. Wang, J. Chang, L. Zhu, X. Li, C. Song, J. Fang, Electron-transport-layer-assisted crystallization of perovskite films for high-efficiency planar heterojunction solar cells, Adv. Funct. Mater. 28 (2018) 1706317, https://doi.org/10.1002/adfm.201706317.
[46] J. Gong, S.B. Darling, F. You, Perovskite photovoltaics: life-cycle assessment of energy and environmental impacts, Energy Environ. Sci. 8 (2015) 1953–1968, https://doi.org/10.1039/C5EE00615E.
[47] A. Gupta, K. Ankireddy, B. Kumar, A. Alruqi, J. Jasinski, G. Gupta, T. Druffel, Intense pulsed light, a promising technique to develop molybdenum sulfide catalysts for hydrogen evolution, Nanotechnology 30 (2019) 175401, https://doi.org/10.1088/1361-6528/aaffac.
[48] J. Bahadur, A.H. Ghahremani, B. Martin, T. Druffel, M.K. Sunkara, K. Pal, Solution processed Mo doped SnO2 as an effective ETL in the fabrication of low temperature planer perovskite solar cell under ambient conditions, Org. Electron. 67 (2019) 159–167, https://doi.org/10.1016/j.orgel.2019.01.027.
[49] R. Dharmadasa, M. Jha, D.A. Amos, T. Druffel, Room temperature synthesis of a copper ink for the intense pulsed light sintering of conductive copper films, ACS Appl. Mater. Interfaces 5 (2013) 13227–13234, https://doi.org/10.1021/am404226e.
[50] R. Dharmadasa, I. Dharmadasa, T. Druffel, Intense pulsed light sintering of electrodeposited CdS thin films, Adv. Eng. Mater. 16 (2014) 1351–1361, https://doi.org/10.1002/adem.201400008.
[51] T. Druffel, R. Dharmadasa, B.W. Lavery, K. Ankireddy, Intense pulsed light processing for photovoltaic manufacturing, Sol. Energy Mater. Sol. Cells 174 (2018) 359–369, https://doi.org/10.1016/j.solmat.2017.09.010.
[52] A.H. Ghahremani, B. Martin, K. Ankireddy, T. Druffel, Rapid processing of perovskite solar cells through pulsed photonic annealing: a review, J. Coat. Technol. Res., 1–6. https://doi.org/10.1007/s11998-019-00217-2
[53] B.W. Lavery, S. Kumari, H. Konermann, G.L. Draper, J. Spurgeon, T. Druffel, Intense pulsed light sintering of CH3NH3PbI3 solar cells, ACS Appl. Mater. Interfaces 8 (2016) 8419–8426, https://doi.org/10.1021/acsami.5b10166.
[54] M. Zhu, W. Liu, W. Ke, S. Clark, E.B. Secor, T.-B. Song, M.G. Kanatzidis, X. Li, M.C. Hersam, Millisecond-pulsed photonically-annealed tin oxide electron transport layers for efficient perovskite solar cells, J. Mater. Chem. 5 (2017) 24110–24115, https://doi.org/10.1039/C7TA07969A.
[55] S. Das, B. Yang, G. Gu, P.C. Joshi, I.N. Ivanov, C.M. Rouleau, T. Aytug, D.B. Geohegan, K. Xiao, High-performance flexible perovskite solar cells by using a combination of ultrasonic spray-coating and low thermal budget photonic curing, ACS Photonics 2 (2015) 680–686, https://doi.org/10.1021/

acsphotonics.5b00119.
[56] L. Qiu, S. He, J. Yang, J. Deng, H. Peng, Fiber-shaped perovskite solar cells with high power conversion efficiency, Small 12 (2016) 2419–2424, https://doi.org/10.1002/smll.201600326.
[57] H. Zhou, Q. Chen, G. Li, S. Luo, T.-b. Song, H.-S. Duan, Z. Hong, J. You, Y. Liu, Y. Yang, Interface engineering of highly efficient perovskite solar cells, Science 345 (2014) 542–546, https://doi.org/10.1126/science.1254050.
[58] K. Ankireddy, A.H. Ghahremani, B. Martin, G. Gupta, T. Druffel, Rapid thermal annealing of CH 3 NH 3 PbI 3 perovskite thin films by intense pulsed light with aid of diiodomethane additive, J. Mater. Chem. 6 (2018) 9378–9383, https://doi.org/10.1039/C8TA01237G.
[59] T. Bu, J. Li, F. Zheng, W. Chen, X. Wen, Z. Ku, Y. Peng, J. Zhong, Y.-B. Cheng, F. Huang, Universal passivation strategy to slot-die printed SnO 2 for hysteresis-free efficient flexible perovskite solar module, Nat. Commun. 9 (2018) 4609, https://doi.org/10.1038/s41467-018-07099-9.
[60] M. Kwoka, L. Ottaviano, M. Passacantando, S. Santucci, G. Czempik, J. Szuber, XPS study of the surface chemistry of L-CVD SnO2 thin films after oxidation, Thin Solid Films 490 (2005) 36–42, https://doi.org/10.1016/j.tsf.2005.04.014.
[61] M.F. Mohamad Noh, N.A. Arzaee, J. Safaei, N.A. Mohamed, H.P. Kim, A.R. Mohd Yusoff, J. Jang, M.A. Mat Teridi, Eliminating oxygen vacancies in SnO2 films via aerosol-assisted chemical vapour deposition for perovskite solar cells and photoelectrochemical cells, J. Alloy. Comp. 773 (2019) 997–1008, https://doi.org/10.1016/j.jallcom.2018.09.273.
[62] L. Wen, B.B. Sahu, J.G. Han, Development and utility of a new 3-D magnetron source for high rate deposition of highly conductive ITO thin films near room temperature, Phys. Chem. Chem. Phys. 20 (2018) 4818–4830, https://doi.org/10.1039/C7CP07318F.
[63] W. Zhang, M. Saliba, D.T. Moore, S.K. Pathak, M.T. Hörantner, T. Stergiopoulos, S.D. Stranks, G.E. Eperon, J.A. Alexander-Webber, A. Abate, Ultrasmooth organic–inorganic perovskite thin-film formation and crystallization for efficient planar heterojunction solar cells, Nat. Commun. 6 (2015) 6142, https://doi.org/10.1038/ncomms7142.
[64] D. Priante, I. Dursun, M. Alias, D. Shi, V. Melnikov, T.K. Ng, O.F. Mohammed, O. Bakr, B.S. Ooi, The recombination mechanisms leading to amplified spontaneous emission at the true-green wavelength in CH3NH3PbBr3 perovskites, Appl. Phys. Lett. 106 (2015), 081902, https://doi.org/10.1063/1.4913463.
[65] J. Shi, H. Zhang, Y. Li, J.J. Jasieniak, Y. Li, H. Wu, Y. Luo, D. Li, Q. Meng, Identification of high-temperature exciton states and their phase-dependent trapping behaviour in lead halide perovskites, Energy Environ. Sci. 11 (2018) 1460–1469, https://doi.org/10.1039/C7EE03543H.
[66] I. Zarazua, J. Bisquert, G. Garcia-Belmonte, Light-induced space-charge accumulation zone as photovoltaic mechanism in perovskite solar cells, J. Phys. Chem. Lett. 7 (2016) 525–528, https://doi.org/10.1021/acs.jpclett.5b02810.
[67] I. Zarazua, G. Han, P.P. Boix, S. Mhaisalkar, F. Fabregat-Santiago, I. Mora-Seró, J. Bisquert, G. Garcia-Belmonte, Surface recombination and collection efficiency in perovskite solar cells from impedance analysis, J. Phys. Chem. Lett. 7 (2016) 5105–5113, https://doi.org/10.1021/acs.jpclett.6b02193.
[68] J. Bahadur, A.H. Ghahremani, B. Martin, S. Pishgar, T. Druffel, M.K. Sunkara, K. Pal, A study on the material characteristics of low temperature cured SnO_2 films for perovskite solar cells under high humidity, J. Mater. Sci.: Mater. Electron. 30 (2019) 18452–18461.